

Modeling Equal and Unequal Mass Binary Neutron Star Mergers Using Public Codes

Roberto De Pietri, Alessandra Feo, and Francesco Maione

Parma University and INFN Parma, Parco Area delle Scienze 7/A, I-43124 Parma (PR), Italy

Frank Löffler

Center for Computation & Technology, Louisiana State University, Baton Rouge, LA 70803 USA

(Dated: February 16, 2016)

We present three-dimensional simulations of the dynamics of binary neutron star (BNS) mergers from the late stage of the inspiral process up to ~ 20 ms after the system has merged, either to form a hyper-massive neutron star (NS) or a rotating black hole (BH). We investigate five equal-mass models of total gravitational mass 2.207, 2.373, 2.537, 2.697 and 2.854 M_{\odot} , respectively; and four unequal mass models with $M_{\text{ADM}} \simeq 2.53 M_{\odot}$ and $q \simeq 0.94, 0.88, 0.83, \text{ and } 0.77$ (where $q = M^{(1)}/M^{(2)}$ is the mass ratio). We use a semi-realistic equation of state (EOS), namely the seven-segment piece-wise polytropic SLyPP with a thermal component given by $\Gamma_{th} = 1.8$. We have also compared the resulting dynamics (for one model) using both, the BSSN-NOK and CCZ4 methods for the evolution of the gravitational sector, and also different reconstruction methods for the matter sector, namely PPM, WENO and MP5. Our results show agreement and high resolution, but superiority of BSSN-NOK supplemented by WENO reconstruction at lower resolutions.

One of the important characteristics of the present investigation is that for the first time, it has been done using only publicly available open source software: the Einstein Toolkit code, deployed for the dynamical evolution; and the LORENE code, for the generation of the initial models. All of the source code and parameters used for the simulations have been made publicly available. This not only makes it possible to re-run and re-analyze our data, but also enables others to directly build upon this work for future research.

PACS numbers: 04.25.D-, 04.40.Dg, 95.30.Lz, 97.60.Jd

I. INTRODUCTION

The new generation of ground-based laser interferometer gravitational wave observatory Advanced LIGO [1] and Advanced Virgo [2] have just now opened a new window in the Universe with the first detection [3] of Gravitational Waves (GW) emitted by the merger of two black holes. Among other likely sources of GW signals in the sensitive frequency band of (40 – 2000) Hz are signals from binary neutron star (BNS) mergers, with expected event rates reaching $\approx 0.2 - 200$ per year between 2016 – 19 [4, 5]. Signals from these events are expected to contain the signature of the equation of state (EOS) governing matter at nuclear density.

In the description of the BNS mergers are involved essentially three stages, the inspiral, the merger and the final evolution to its final state (post-merger stage) that would quite likely be a final black hole (BH) surrounded by an accretion disk. The inspiral phase can be modeled with good accuracy by post-Newtonian calculations and, in particular, using the Effective One Body (EOB) approach [6]. They are capable of producing accurate waveforms up to a time very close to the merger. More recently, the EOB approach started to be used to model tidal corrections [7, 8]. These analytic techniques are useful for quickly computing waveform templates to matched filtering searches in GW detector data analysis. The role of Numerical Relativity (NR) in this regime is mainly to test and help improve the properties of these analytic techniques. However, one has to keep in mind that

such comparison and improvement would need the use of NR data extrapolated at infinite resolutions or at a resolution where discretization errors are negligible. To do this analysis, the convergence properties of the used code during the inspiral phase needs to be known. For the post-merger stage, NR is the only available investigation tool to confront the experimental result that would be obtained by a successful LIGO/VIRGO detection with the underlying physics of neutron stars (NS). As pointed out in [9, 10] and in references therein, an accurate description of the GW emission of different model sources (models inferred by different choice of the underlying NS physics through different choices of EOS) are useful for developing empirical relations to be able to infer NS parameters from future GW detections as well as to get information on the correct EOS that describe matter at these extreme conditions.

In this work, we concentrate on the information that can be extracted from BNS simulations using the SLy EOS [11], where a semi-realistic seven-segment piece-wise (isentropic)-polytropic approximant [12], namely the SLyPP EOS, is used and whose different parameters are reported in Table I. Such an approximant covers the whole range of density simulated, starting from the NR *atmosphere* of $6.18 \cdot 10^6 \text{ g/cm}^3$ up to the density in the interior of the NS supplemented by an artificial thermal component to ensure that the hydro-dynamical evolution is consistent with the Energy-Momentum tensor conservation. To such extent, we simulated five equal mass BNS systems and four unequal mass systems, and for each of these systems we simulated the late-inspiral

phase (last three to five orbits, depending on the model) and post-merger using at least three different resolutions and the state-of-the-art WENO fifth-order reconstruction method [13, 14]. We evolved the gravitational part of the system using the well-tested BSSN-NOK evolution scheme [15–19]. For one BNS system, we also compared the evolution using different reconstruction methods (PPM and MP5, in addition to WENO) and a different spacetime evolution scheme: CCZ4 [20]. We checked the influence of the EOS by simulating BNS models that have the same total baryonic mass but different EOS, in our case two simple one-piece (isentropic)-polytropic EOSs with different stiffness ($\Gamma = 2.75$ and $\Gamma = 3.00$). We did a complete convergence analysis of the computed merger times of the BNS as a function of the resolution in the case of WENO and PPM reconstruction (using BSSN-NOK evolution for the gravitational sector).

The organization of the paper is as follows. In Sec. II we describe the properties of the BNS systems investigated in the present work, and we review the numerical setup used. In Sec. III we present and discuss our results. Conclusions that can be drawn from the present investigation are given in Sec. IV and, finally, the computational cost of the simulations is discussed in the appendix.

Throughout this paper we use a space-like signature $- , + , + , +$, with Greek indices running from 0 to 3, Latin indices from 1 to 3, and the standard convention for summation over repeated indices. The computations are performed using the standard 3+1 split into (usually) space-like coordinates $(x, y, z) = x^i$ and a time-like coordinate t . Our coordinate system $(x^\mu) = (t, x^i) = (t, x, y, z)$ (far from the origin) has, as it can be checked, almost isotropic coordinates and far from the origin they would have the usual measure unit of “time” and “space”. In particular, t is time when measured from an observer at infinity.

All computations have been done in normalized computational units (hereafter denoted as CU) in which $c = G = M_\odot = 1$. We report all results in cgs units except for values of the polytropic constant K , whose unit of measurement depends on the value of the dimensionless polytropic exponent Γ , so we report K in the above defined normalized unit CU). CU are also used to denote resolutions, e.g., $dx = 0.25$ CU, and there they mean the resolution on the finest grid at initial time (which for most cases is the same for the entire evolution). We also report masses in terms of the solar mass M_\odot . The reader should note that, as is usual in most of the work on this subject, we describe matter using the variable ρ (baryon mass density), ϵ (specific internal energy) and P , instead of the typical notation used in astrophysics, $\bar{\rho}$ (energy density), \bar{n} (baryon number density) and P . Their relation is the following: $\bar{\rho} = e = \rho(1 + \epsilon)$ and $\bar{n} = \rho/m_B$ (m_B is the baryon mass).

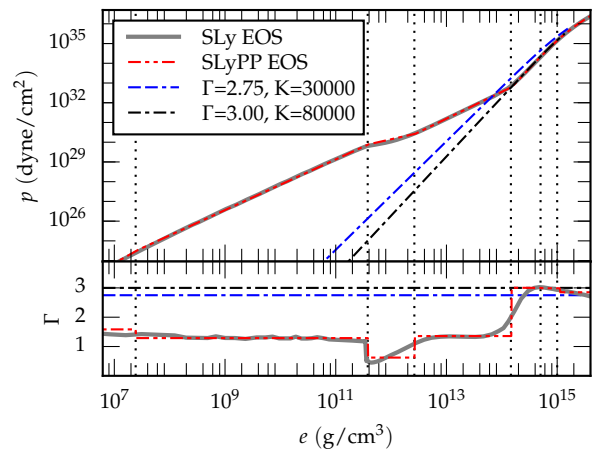


FIG. 1. Plot of the pressure (P) and of the adiabatic index ($\Gamma = d \log(P)/d \log(\rho)$) as a function of the energy density ($e = \rho(1 + \epsilon)$) for the SLy EOS, its piece-wise polytropic approximation (the one used in the present work) and two isentropic polytropic EOS $P = K\rho^\Gamma$.

i	Γ_i	ρ_i (CU)	ρ_i (g/cm^3)
0	1.58425	1×10^{-11}	$\simeq 6.18 \times 10^6$
1	1.28733	3.951156×10^{-11}	$\simeq 2.43 \times 10^7$
2	0.62223	6.125960×10^{-7}	$\simeq 3.78 \times 10^{11}$
3	1.35692	4.254672×10^{-6}	$\simeq 2.63 \times 10^{12}$
4	3.005	2.367449×10^{-4}	$\simeq 1.46 \times 10^{14}$
5	2.988	8.114721×10^{-4}	$\simeq 5.01 \times 10^{14}$
6	2.851	1.619100×10^{-3}	$\simeq 1.00 \times 10^{15}$

TABLE I. Parameters used for the seven-segment piece-wise polytropic SLyPP EOS (see [12]) used to represent the SLy EOS described in [11]. The thermal component is described by $\Gamma_{th} = 1.8$. The values K_i are chosen using $K_0 = 1.685819 \times 10^2$ CU while the remaining values K_i (with $i > 0$) are calculated to produce a continuous EOS. The value ρ_0 is the setting of the atmosphere used in our simulations.

II. INITIAL MODELS AND NUMERICAL METHODS

In the present work we have analyzed the dynamics of the merger of two NSs from the late stage of the inspiral process to around 20 ms after the system has merged to form a hyper-massive NS or a rotating BH. To be properly described, such a system needs the use of the Einstein’s GR equations to describe the metric ($g_{\mu\nu}$) of the dynamical spacetime and a proper treatment for the description of matter (see [21] for more details on the employed equations). For describing the matter present in the system we use its perfect-fluid approximation, and close the system of evolution equations using an EOS of the form $P = P(\rho, \epsilon)$, where P is the pressure, ρ is the rest mass density, and ϵ is the specific internal energy of the matter. In the present work we used a seven-segment isentropic polytropic approximant (what we refer to here as SLyPP) of the widely used SLy EOS

prescription [11] supplemented by a thermal component described by $\Gamma_{\text{th}} = 1.8$ (see and Figure 1).

More precisely, $P(\rho, \epsilon) = P_{\text{cold}}(\rho) + P_{\text{th}}(\rho, \epsilon)$, and in each density region $\rho_i \leq \rho < \rho_{i+1}$:

$$P_{\text{cold}} = K_i \rho^{\Gamma_i} \quad (1)$$

$$\epsilon_{\text{cold}} = \epsilon_i + \frac{K_i}{\Gamma_i - 1} \rho^{\Gamma_i - 1} \quad (2)$$

$$P_{\text{th}} = \Gamma_{\text{th}} \rho (\epsilon - \epsilon_{\text{cold}}), \quad (3)$$

where ϵ_i and K_i are chosen to ensure the pressure and specific energy density continuity. Fig. 1 shows a plot of the pressure (P) and of the adiabatic index (Γ) as a function of the energy density e for the SLy EOS (gray line) [11] and its piece-wise polytropic approximation, used in the present work (dashed red line, SLyPP) [12] supplemented by a thermal component $\Gamma_{\text{th}} = 1.8$. Also shown are two often-used isentropic EOS with $P = K\rho^\Gamma$, $\Gamma \in \{2.75, 3.00\}$. These can be seen as a single-piece approximant of the same SLy EOS (see [22, 23]), and have been used for test cases here. The exact parameters of the seven-segment isentropic polytropic approximant are shown in Table I and, as can be seen in the panels of Fig. 1 where the vertical dots lines shown the transition of the approximant between the various region, they represent various physically distinct parts of the star.

Following the discussion of [24] we have chosen to use the arbitrary choice of $\Gamma_{\text{th}} = 1.8$. This choice has a few drawbacks, the main one being that in the low-density region it should approach $4/3$, since there the pressure is provided primarily by an ideal gas of ultra-relativistic electrons and photons, so we overestimate the pressure support. On the other hand (see [24]), a value of $\Gamma_{\text{th}} = 2.0$ seems to be too high, while a value of $\Gamma_{\text{th}} = 1.5$ might yield a too low pressure support in the core.

All equations are solved as evolution equations with respect to a coordinate time t , using the common 3+1 decomposition of space-time (see [21] and references therein for details and notation).

The initial data of our simulations is calculated using the LORENE code [25, 26] that provides the possibility to generate arbitrary initial data for irrotational BNS.

The properties of the initial data we simulated are summarized in Table II where are reported, for each model, the baryonic masses of the two stars ($M_0^{(1)}$, $M_0^{(2)}$), their gravitational masses ($M^{(1)}$, $M^{(2)}$) at infinite separation, the initial rotational angular velocity (Ω), and the total mass (M_{ADM}) and angular momentum (J). All these models were generated to be at a relative physical distance of 40 km. We generated five equal-mass models of total gravitational mass 2.207, 2.373, 2.537, 2.697 and $2.854M_\odot$, respectively, and four unequal mass models with $M \simeq 2.53 M_\odot$ and $q \simeq 0.94, 0.88, 0.83$, and 0.77 (where $q = M^{(1)}/M^{(2)}$).

One of the main characteristics of the present investigation is that it can be reproduced using only freely avail-

name	$M_0^{(1)}$	$M_0^{(2)}$	$M^{(1)}$	$M^{(2)}$	Ω	M_{ADM}	J
	$[M_\odot]$	$[M_\odot]$	$[M_\odot]$	$[M_\odot]$	$[\frac{\text{krad}}{\text{s}}]$	$[M_\odot]$	$[\frac{GM_\odot^2}{c}]$
SLy12vs12	1.20	1.20	1.11	1.11	1.932	2.207	5.076
SLy13vs13	1.30	1.30	1.20	1.20	1.989	2.373	5.730
SLy14vs14	1.40	1.40	1.28	1.28	2.040	2.536	6.405
SLy15vs15	1.50	1.50	1.36	1.36	2.089	2.697	7.108
SLy16vs16	1.60	1.60	1.44	1.44	2.134	2.854	7.832
SLy135vs145	1.35	1.45	1.24	1.32	2.040	2.536	6.397
SLy13vs15	1.30	1.50	1.20	1.36	2.040	2.535	6.376
SLy125vs15	1.25	1.55	1.16	1.40	2.040	2.533	6.337
SLy12vs16	1.20	1.60	1.11	1.44	2.039	2.531	6.281
G275th14vs14	1.40	1.40	1.29	1.29	2.053	2.554	6.513
G300th14vs14	1.40	1.40	1.26	1.26	2.028	2.498	6.243

TABLE II. Properties of the initial irrotational BNS models simulated in the present work. All these models were generated using the public LORENE code [26]. The columns show, in this order, the baryonic masses of the two stars ($M_0^{(1)}$, $M_0^{(2)}$), their gravitational masses ($M^{(1)}$, $M^{(2)}$) at infinite separation, the initial rotational angular velocity (Ω), the total initial ADM mass (M_{ADM}), and the angular momentum (J). The notation for the model names is as in the following example: SLy13vs15 denotes the SLyPP EOS and baryonic masses equal to $1.3M_\odot$ and $1.5M_\odot$, respectively, while, G275th14vs14 means polytropic (Γ -law) EOS with $\Gamma = 2.75$.

able open source software. The GNU licensed LORENE code [26] has been used for generating the initial condition, and the Einstein Toolkit [21, 27] was deployed for the dynamical evolution. The Einstein Toolkit is a free, publicly available, community-driven general relativistic (GR) code. In particular we have chosen the eleventh release (code name ‘‘Hilbert’’, ET_2015_05). Some local modification and additions were necessary, all of which are open-source and freely available from the gravity SVN server of Parma University, and all of which are planned to be proposed to be in the next release of the Einstein Toolkit (see appendix).

The Einstein Toolkit is based on the Cactus Computational Toolkit [28–30], a software framework for high-performance computing (HPC). Its main tools used in the present study are:

- The adaptive mesh refinement (AMR) methods implemented by **Carpet** [31–33].
- Hydrodynamic evolution techniques provided by the **GRHydro** package [34–36].
- The evolution of the spacetime metric handled by the **McLachlan** package [37]. This code is auto-generated by Mathematica using **Kranc** [38–40], implementing the Einstein equations via a $3+1$ -dimensional split using the BSSN-NOK formalism [15–19] and CCZ4 [20].

All the main properties used in the deployed code are described in much more detail in [23] for the Einstein Toolkit in general, in [36] for especially some details

about the hydrodynamics, and in [22, 23] for similar usage in previous work. In particular:

- We used a fourth-order Runge-Kutta [41, 42] method with Courant factor 0.25. Kreiss-Oliger dissipation was applied to the curvature evolution quantities in order to damp high-frequency noise.
- We use fourth-order finite difference stencils for the curvature evolution, $1 + \log$ [19] slicing, and a Γ -driver shift condition [19]. During evolution, a Sommerfeld-type radiative boundary condition is applied to all components of the evolved BSSN-NOK variables as described in [18].
- The HLLE (Harten-Lax-van Leer-Einfeldt) approximate Riemann solver [43, 44] is used. The main reason for this choice is that we are evolving also the magnetic field (even if it is set to zero).
- An artificial low-density atmosphere with $\rho_{\text{atm}} = 10^{-11}$ CU is used, with a threshold of $\rho_{\text{atm_reset}} = 1.01 \times 10^{-11}$ CU below which regions are set to be atmosphere. Hydrodynamical quantities are also set to be atmosphere at the outer boundary.
- All evolutions presented here use a mirror symmetry across the (x, y) plane, consistent with the symmetry of the problem, which reduces the computational cost by a factor of 2.
- We use mesh refinement, with a fixed box-in-box topology for all simulations except otherwise noted. The boundaries of the six levels (seven for simulations involving a final black hole) are indicated in Tab. V.
- Different reconstruction methods have been used, and their effects on the results are shown in Sec. III. The reconstruction method used for most of the simulations is the essentially non-oscillatory method WENO (5th order weighted-ENO) [13, 14], while the other reconstruction methods employed are PPM (the piece-wise parabolic reconstruction method) [45], and MP5 (5th order monotonicity preserving) [46].
- In contrast to [21] and [22, 23] we reconstruct instead of the three-velocity the product of the three-velocity and the Lorentz factor to prevent artificial velocities exceeding the speed of light due to numerical errors.

The computational cost of the simulation is described in the appendix A and shown in Table VI, and it is almost the same in the case of using different reconstruction methods (WENO, PPM, MP5) or in the case of the CCZ4 method for the evolution of the gravitational sector. From the data shown in Table VI one may note that simulations with resolution $dx = 0.75$, CU can be performed on a workstation while a whole simulation of a

model at resolution $dx = 0.25$ CU will need current computational resources comparable to 256 cores for 6 days.

As will be shown in the next section, the fact that our code gives a reasonable numerical result at very coarse resolution such as $dx = 0.75$, CU has been very valuable in setting the details of the simulations and on the specific choice of the initial model to be studied.

III. RESULTS

The general characteristics of the evolution of the systems is shown (for model SLy14vs14, where 14vs14 stands for baryon masses $1.4M_{\odot}$) in Figure 2, where we plotted the density in the $x-y$ plane during various stages of the evolution. In the top panel the initial configuration is shown, alongside a snap-shot depicting a sensible tidal-deformation and the start of the actual merger phase, which then proceeds on the middle panel. The after-merger relaxation phase can be seen at the bottom panel, until the end of the simulation.

The overall process is associated with emission of gravitational radiation and a consequent loss of energy and angular momentum associated to such emission. The procedure we follow to extract this information is described in detail in the following (subsection III A). In the case of model SLy14vs14 we have found that the maximum signal we obtain is in the h_{22} component of the GW signal, with the total amount of energy extracted from the GW emission being of the order of $0.08 M_{\odot}c^2$. The loss of angular momentum (in the z component) is of the order of $2 M_{\odot}^2G/c$ (see Figure 3). Note especially that there is a clear peak on the amplitude of the GW signal (h_{22}), which will later be used as an indication of the merger time.

A. Gravitational Wave Signal Extraction

From each simulation, we extracted the GW signal using both the curvature-perturbation theory based on the Newman-Penrose scalar ψ_4 [47] and the Regge-Wheeler [48] and Zerilli [49] theory of metric-perturbations of the Schwarzschild spacetime, in the gauge-invariant formulation by Moncrief [50].

The Newman-Penrose scalar ψ_4 is calculated by the Einstein Toolkit module `WeylSca14`, following the prescription of [51], and is decomposed in spin-weighted spherical harmonics of spin -2 by the module `Multipole`:

$$\psi_4(t, r, \theta, \phi) = \sum_{l=2}^{\infty} \sum_{m=-l}^l \psi_4^{lm}(t, r) {}_{-2}Y_{lm}(\theta, \phi). \quad (4)$$

We extracted ψ_4 components up to $l = 5$. ψ_4 is linked to the GW strain by the following relation, formally valid only at spatial infinity:

$$\psi_4 = \ddot{h}_+ - \ddot{h}_x \quad (5)$$

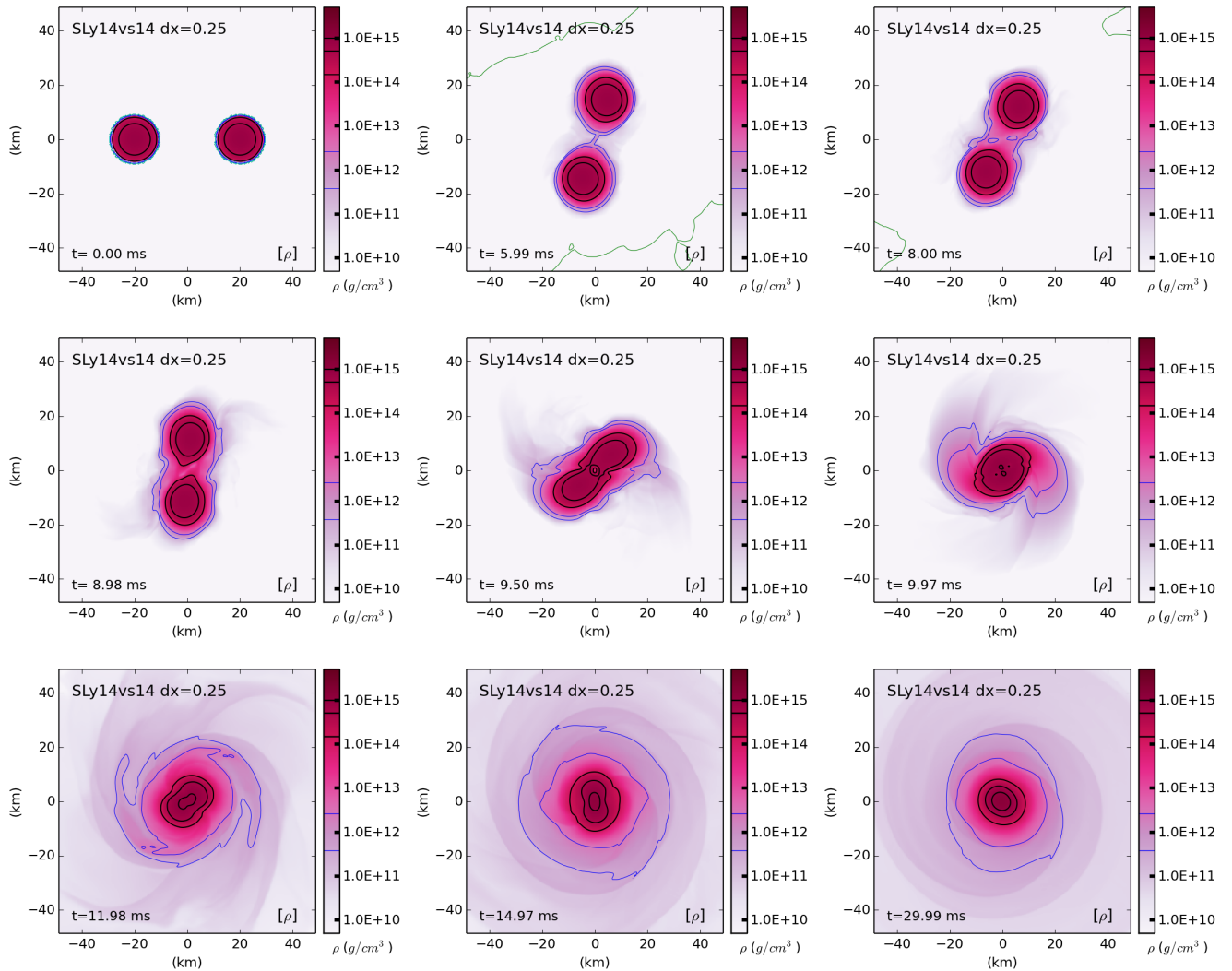


FIG. 2. Dynamics of the evolution of model SLy14vs14. Shown using a color gradient is the evolution of the matter density (ρ) at various times. The isocontour lines denote the transition of the various pieces of the polytropic isentropic approximant of the SLyPP EOS. The more external, blue isocontour represents the neutron-drip (ρ_2) density.

We therefore need to integrate each component of ψ_4^{lm} twice in time to get h^{lm} . We performed those integrations numerically in the time domain using a simple trapezoidal rule.

$$\tilde{h}_{lm}^{(0)}(t) = \int_0^t dt' \int_0^{t'} dt'' \psi_4^{lm}(t'', r). \quad (6)$$

Please note that here we defined the $\tilde{h}_{lm}^{(0)}$ quantities in the coordinate time of the detector and not with respect to the retarded time t_{ret} (see below for the definition of the retarded time) at the location of the detector. Following the discussion of [52], we integrated the signal twice from coordinate time $t = 0$ and not from the zero of the retarded time (t_{ret}) at the detector. We then perform a linear fit of the strain $\tilde{h}_{lm}^{(0)}$ and subtracted its result to

the integrated signal to obtain

$$\tilde{h}_{lm} = \tilde{h}_{lm}^{(0)} - Q_1 t - Q_0, \quad (7)$$

where the fit parameters have a clear physical interpretation as $Q_1 = \dot{\tilde{h}}(t = 0)$ and $Q_0 = \tilde{h}(t = 0)$.

However, we found that the free choice of integration constants is not very effective in eliminating the initial spurious radiation. The choice of starting the integral from $t = 0$ in coordinate time may be useful if complex fitting procedures are used, or if the simulation time of the data is short; but this is not the case for the present simulations. Starting the integral from $t = 0$ also has the advantage of much smaller values of Q_1 and Q_0 to recover with the fitting procedure, thus reducing the fit errors.

On the other hand, integrating from zero retarded time instead leads to unphysical amplitude oscillations in the

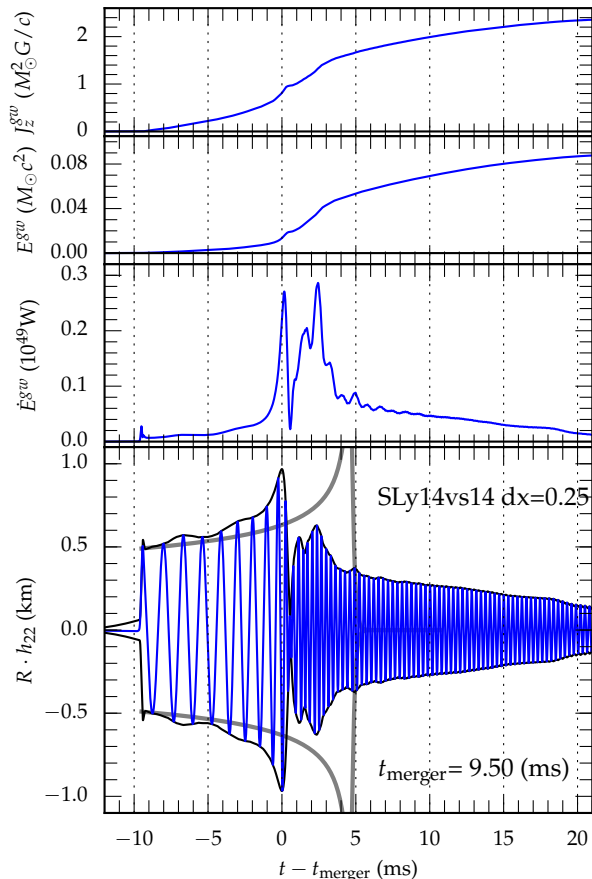


FIG. 3. Results for the evolution for model SLy14vs14 at resolution $dx = 0.25$ CU. The two top panels show the total angular momentum and total energy momentum carried away by gravitational radiation. The third panel depicts the total GW luminosity (energy flux). Finally, the bottom panel shows the envelope of the GW amplitude and its real part, multiplied by the distance of the observer to the origin. The thick gray line shows the envelope of the signal expected from a binary black hole (BBH) system of the same masses (see text).

first 4 ms of the inspiral. These are not present with our final integration procedure and also not in the signal from the Regge-Wheeler-Zerilli variables, which do not require integrations. The resulting waveforms obtained with the procedure described above show a left-over non-linear drift in $h(r, t)$, that was attributed in [53] to unresolved high-frequency noise aliased in the low-frequency signal that does not result in a zero average in the double integration. Instead of adopting the fixed-frequency integration method recommended in [53] (which we found to be too sensible to the low-frequency cutoff choice) we performed a fit to a second order polynomial as already done in [54], obtaining:

$$\tilde{h}_{lm} = \tilde{h}_{lm}^{(0)} - Q_2 t^2 - Q_1 t - Q_0. \quad (8)$$

We found that this is sufficient to eliminate most of the non-physical drift in the signal, at least for the dominant $l = 2, m = \pm 2$ modes responsible for almost all of the radiated energy and angular momentum. For higher multipoles, even higher-order fitting polynomials may be used to reduce the drift, as already observed in [55]. However, we did find that the use of such a higher-order fitting polynomial is not sufficient to eliminate the residual drift still present, and we find no advantage in applying such procedure. We instead stick to use only second-order polynomials where the additional Q_2 constant may be interpreted as an offset constant value due to the fact that the $\psi_4^{lm}(t = 0)$ is extracted at a finite radius and not at or close to infinity.

For our simulations, we also used the GW extraction from the Regge-Wheeler (odd, ψ^o) and Zerilli (even, ψ^e) functions that are computed by the code `WaveExtract` and are related to the GW strain (in our normalization) by:

$$\hat{h}_{lm} = \frac{1}{r\sqrt{2}} (\psi_{lm}^e + i\psi_{lm}^o), \quad (9)$$

where r is the Schwarzschild coordinate, while our standard NR coordinates (R, θ, ϕ) are asymptotically similar to isotropic coordinates [56] and we have the following expression for

$$R = r \left(1 + \frac{M_{\text{ADM}}}{2r} \right)^2, \quad (10)$$

$$t_{\text{ret}} = R^* = R + 2M_{\text{ADM}} \log \left(\frac{R}{2M_{\text{ADM}}} - 1 \right), \quad (11)$$

where r is the coordinate radius, t is the coordinate time and M_{ADM} is the initial ADM mass of the system (see table II). We also checked that the resulting r agrees with the areal radius $R = \sqrt{A(r)/4\pi}$, where $A(r)$ is the surface of the sphere of constant coordinate radius (r) that is derived using such extraction. We found the relative difference between the measured values of R and M_{ADM} from the simulation and the values used in Eqs. at coordinate time $t = 0$, to be a few parts over 10^{-4} , for a detector at coordinate radius $r = 700$ CU.

We extracted the GW signal at 13 different coordinate radii from $r = 100$ CU to $r = 700$ CU to check its convergence and whether the extraction at the outermost radius is a sufficient approximation of the theoretically necessary extraction at spatial infinity. In the following, we do not develop a full discussion of the convergence properties of the extraction at different radii or the comparison of different extraction methods; we limit our work here to the representative model SLy14vs14. Here, the signals $R\tilde{h}_{22}(t - R^*) = R\tilde{h}_{22}(t - t_{\text{ret}})$, computed at coordinate radii $r = 700$ CU and $r = 650$ CU agree with an error of the order of 1% during the entire simulation. We also found that the amplitude and the phase of the signal extracted at different radii were scaling better with

ψ_4 than with the Regge-Wheeler and Zerilli (RWZ) extraction. The RWZ waveforms showed also unphysical amplitude oscillations in the final part of the signal. For these reasons, all the amplitudes and signals discussed in the present work will refer to extraction based on ψ_4 , performed at coordinate radius $r = 700$ CU, and we use

$$Rh_{lm}(t) = R\tilde{h}_{lm}(t - t_{\text{ret}}) \quad (12)$$

where R and t_{ret} are the radius and retarded time at which the GW signal is extracted, computed using Eqs. (10,11). This corresponds to the GW signal as measured at unit distance and as if the signal would have been emitted at the coordinate origin.

From the GW signal we were able to compute the radiated energy, angular momentum and linear momentum fluxes, following the procedure described in [57]. We arrive at the final expression for the complex GW signal on a spherical surface at radius r :

$$h(t, \theta, \phi) = \sum_{l=2}^{\infty} \sum_{m=-l}^l h_{lm}(t) {}_{-2}Y_{lm}(\theta, \phi). \quad (13)$$

In the results presented here, this quantity refers to the extraction radius $r = 700$ CU, and the sum over l is limited to $l = 2 \dots 5$, as that is the maximum l for which we extract components. The above expression for the gravitational signal allows to obtain the final equations:

$$\frac{dE^{gw}}{dt} = \frac{R^2}{16\pi} \int d\Omega |\dot{h}(t, \theta, \phi)|^2 \quad (14)$$

$$\frac{dJ_z^{gw}}{dt} = \frac{R^2}{16\pi} \text{Re} \left[\int d\Omega \left(\partial_\phi \dot{h}(t, \theta, \phi) \right) h(t, \theta, \phi) \right] \quad (15)$$

where $\dot{h}(t, \theta, \phi)$ is the derivative with respect to t of $h(t, \theta, \phi)$ and R is the physical radius of the extraction sphere.

The above procedure allows us to define the merger time (t_{merger}) as the time for which we have the maximum of the 22-component of the GW signal (h_{22}). Clearly, values defined in this way depend on the resolutions used to perform the simulation and on the accuracy of the employed simulation method. A detailed study of the convergence of the simulation methods used is of paramount importance.

B. Accuracy in the Determination of Merger Time

The code we use (GRHydro), as discussed previously, allows the use of different reconstruction methods for the hydrodynamics sector (among others: WENO, PPM and MP5). We also have the potential to use an alternative scheme for the integration of the gravitational sector, namely CCZ4. Different choices in numerical methods

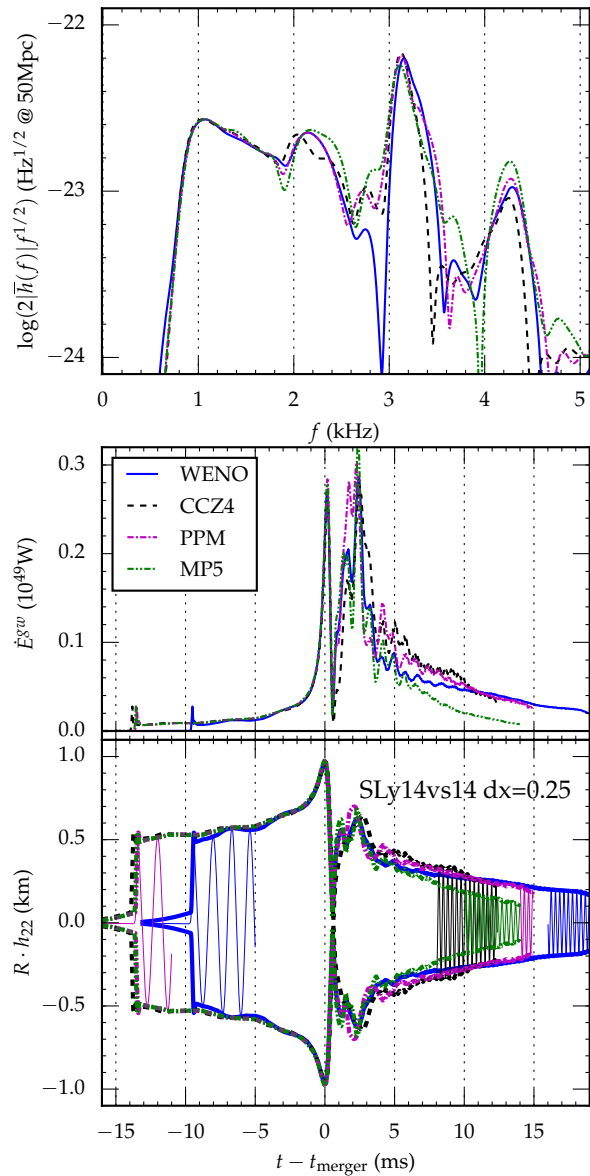


FIG. 4. Comparison of the evolution of model SLy14vs14 at resolution $dx = 0.25$ CU, using different reconstruction methods for the hydrodynamics equations and different evolution schemes for the gravitational sector. Quantities are aligned in time at their respective (different) merger times. The upper panel shows the power spectral density (PSD= $2|\bar{h}(f)| \cdot f^{1/2}$) of the effective GW signal in the optimally oriented case for a source at 50 Mpc, where it is considered the signal from $t_{\text{merger}} - 9$ ms to $t_{\text{merger}} + 11$ ms and a Blackman-windowing function has been applied. The second panel shows the total GW luminosity (energy flux). Finally, the bottom panel shows the envelop of the gravitational wave amplitudes and their real parts, multiplied by the distance to the observer. Please note that the evolutions are all similar to each other, and they differ mainly in the merger time, but not that much in the amount of total energy carried away by GW in this stage, and also not in the damping time of the final excitation of the merger remnant.

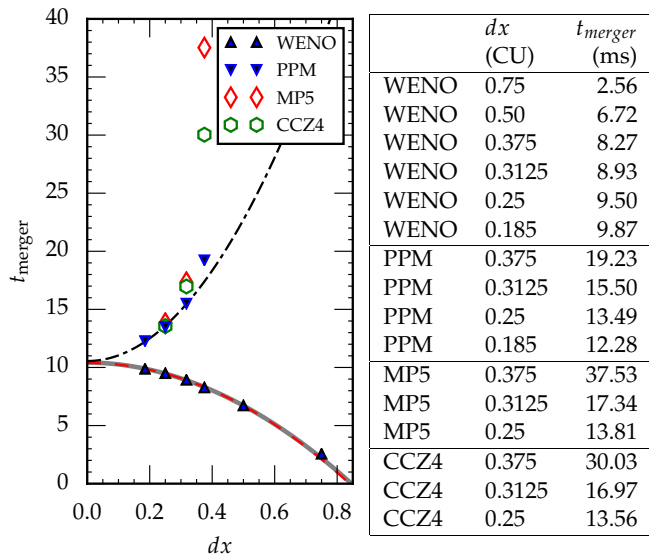


FIG. 5. Fits of the merger time t_{merger} as a function of the resolution dx using the PPM (dashed-dot black line) and the WENO (dashed red line) reconstruction methods, and the BSSN-NOK evolution method for the gravitational variable assuming second order convergence. In the case of WENO reconstruction we also report (thick gray line) the fit where the convergence order $\gamma = 1.96 \pm 0.14$. The values of the merger time extrapolated to $dx = 0$ are 10.39 ± 0.03 and 10.55 ± 0.20 for WENO and PPM data, respectively. Please note that the two fits corresponding to the WENO data are so close that they are on top of each other here.

may lead not only to different orders of convergence, but also to different ranges of convergence even for methods with the same convergence order. To investigate the effect of different numerical methods on the errors (especially in the determination of merger time) and gain confidence in the obtained results, we simulated the same model (SLy14vs14) using different combinations of numerical methods, but keeping all other parameters the same. The different combinations were:

- (i) WENO reconstruction and BSSN-NOK scheme for the gravitational sector;
- (ii) PPM reconstruction and BSSN-NOK scheme for the gravitational sector;
- (iii) MP5 reconstruction and BSSN-NOK scheme for the gravitational sector;
- (iv) WENO reconstruction and CCZ4 scheme for the gravitational sector.

The first result we report here is that, as shown in Fig. 4, all four combinations describe the same dynamics, for a resolution $dx = 0.25$ CU. However, from a single resolution alone a possibly different degree of accuracy cannot be deducted. Therefore, we have examined the four different aforementioned combinations of numerical methods at various resolutions in the range $dx = 0.75, \dots, 0.185$ CU and focused the analysis on the pre-merger stage. For each resolution, we performed a full simulation and computed the merger time (t_{merger}). Clearly all the values we obtained are an approxima-

tion of the “true” merger time of the system, but differences between numerical methods and trends for different resolutions can be observed. For example, in the case of the standard setup used in this work (WENO and BSSN-NOK), t_{merger} ranges from 2.95 ms at a very coarse $dx = 0.75$ CU resolution to 9.86 ms at the highest resolution used ($dx = 0.185$ CU, about three times more expensive to perform than the reference resolution $dx = 0.25$).

We also found that simulations of model SLy14vs14 do not merge (within a simulation time of 30 ms), contrary to what we found using WENO and BSSN-NOK, at all the other three combinations of evolution methods, when using resolution coarser than or equal to $dx = 0.50$ CU. A full table of the computed merger times is shown in Figure 5 where we also plot the merger time vs. resolution for all four choices of numerical methods. The figure clearly shows that the combination WENO and BSSN-NOK performs much better at lower resolutions, at least for systems like the one we investigate here. In practice, using our standard setup, we obtained reasonable merger properties even at a very low resolution of $dx = 0.50$ CU and, in some cases, at least qualitative agreement using a resolution as low as $dx = 0.75$ CU. This simulation can be performed on a laptop.

The fact that a WENO-CCZ4 evolution needs a higher resolution than the WENO-BSSN-NOK may be due to the fact that the Hamiltonian constraint (even if damped) enters in the evolution equations of the CCZ4 system, while this is not the case for the BSSN-NOK scheme [20]. It was also pointed out in [58] that CCZ4 may show instability depending on the value of the damping parameter (we used $k_1 = 0.05, k_2 = 0$, for $k_3 = 1$). Our result indicates that a deeper study of the properties of the CCZ4 formulation (and the very similar Z4c formulation [59]) is needed for its use at very low resolution. At the same time, the result that the PPM scheme is less accurate does not come as a surprise, since it is formally a third-order method instead of a fifth-order one (like WENO). The fact that the results for the MP5 reconstruction are worse than the ones for WENO (at the resolutions used here) needs further investigation too, and is left for future work.

Despite all observed differences it is important to make sure that all tested methods lead to the same determination of the “true” merger time, denoted as $t_{\text{merger}}(dx = 0)$ as it is the merger time computed using an unlimited resolution, i.e., $dx = 0$. The results for the determination of the merger using an extrapolation from its values as a function of the resolution are shown in Figure 5. We have found that all data (except when using $dx = 0.75$ CU) show a convergence order of almost exactly two for WENO-BSSN-NOK, which seems to indicate that the main error (for the merger phase) is dominated by a second-order method. If we fit the merger time as a function of the used resolution ($t_{\text{merger}}(dx)$) and assume the following dependence: $t_{\text{merger}}(dx) = t_{\text{merger}}^{dx=0} + A \cdot dx^\gamma$, we obtain $t_{\text{merger}}^{dx=0} = (10.42 \pm 0.10)$ ms and $\gamma = 1.95 \pm 0.12$,

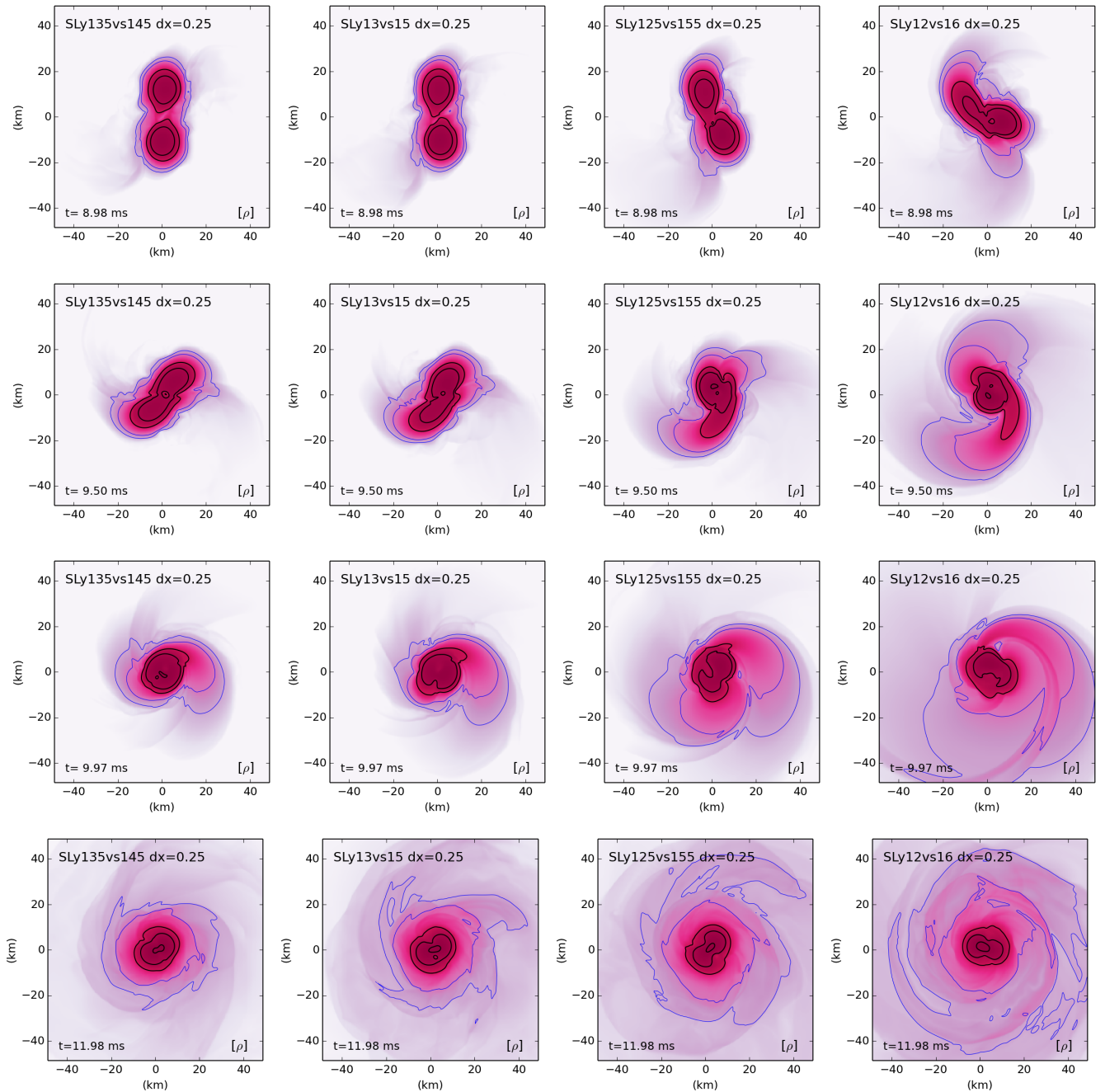


FIG. 6. Snapshot of the dynamics (in the merger phase) of the evolution of the four unequal mass models at resolution $dx = 0.25$ CU. The density color codes and the isocontours are the same of Figure 2.

which is consistent with the assumption of a second-order convergence for the simulation of the merger phase. A similar analysis for WENO-BSSN-NOK results in a similar convergence rate and merger time. However, more simulations of higher resolution would be necessary for the other two possibilities, MP5-BSSN-NOK and WENO-CCZ4. Since we find agreement between the extrapolated time using the combination WENO-BSSN-NOK and PPM-BSSN-NOK already for moderate resolution, we decided not to push this analysis forward for

the other two methods due to the low impact of the result on this work compared to the high computational cost.

We cannot currently explain with certainty why the merger-time increases with resolution for WENO+BSSN, while this is different for other combinations of numerical methods. A similar trend has also been reported in [60], where an adapted version of Z4c method and a Kurganov-Tadmor scheme [61] with PPM interpolation for matter evolution have been used. In [62] it is asserted that sign differences in the merger time trend for different resolu-

tions between different codes may be due to a different sign of the numerical errors introduced by the various methods, leading to a different effect (in sign) on the dependence of the merger time with respect to resolution.

Of the numerical methods employed in the present paper, the only second-order method is the computation of the flux-vector-splitting, which seems to dominate (in case of WENO reconstruction) the convergence order over all other numerical methods. Higher-order flux-vector-splitting methods exist and have been used in simulations of BNS mergers in recent work [63]. Our study suggests that the combined use of high-order flux-vector-splitting with WENO reconstruction seems to be the most effective numerical method to be used in simulating BNS mergers.

C. General Results for the Properties of the Evolution.

As explained in Section II we evolved eleven different models of BNS systems whose properties are summarized in Table II. The evolution of all models shows the same overall dynamics as that of model SL14vs14 (see Figures 2 and 3) with two notable exceptions: the evolution of model SLy16vs16 which promptly forms a BH after the two stars merge, and the evolution of model SLy15vs15 which shows a delayed BH formation: 7.4 ms after the merger, at resolution $dx = 0.25$ CU. A more detailed discussion of the BH formation properties of these models can be found in subsection III D).

In all other cases, the relatively uneventful inspiral stage is followed by a very dynamical merger phase that can last up to 8 ms and, finally, a relaxation stage where the remaining star shows a single bar-deformed excited state of what will be the final configuration of the system within the simulation time. There is clear evidence that in the merger phase the two-arms structure present in the case of equal mass systems is transformed into a single-arm structure as the mass ratio increases (see Figure 6).

All of the following results have been obtained using WENO reconstruction and the BSSN-NOK scheme for the gravitational sector. We evolved all of the eleven models using at least the three resolutions $dx = 0.5$, 0.375 , and 0.25 CU to be sure of convergence (at least during the inspiral). The results from different resolutions were also used to determine the merger time as an extrapolation at $dx = 0$, as detailed in section III B, using the guess $t_{\text{merger}}(dx) = t_{\text{merger}}^{dx=0} + A \cdot dx^2$ and performing a fit. The results obtained in this way are shown in Table III, where only data at $dx = 0.5$, $dx = 0.375$ and $dx = 0.25$ CU are used for the fit. This includes the computed merger time, the extrapolated merger time, and the statistical estimate of the error, as well as the merger time obtained from an effective one-body (EOB) [64] waveform, corresponding to a BBH system of the same gravitational mass that is, at $t = 0$, rotating with

name	$t_{\text{merger}}^{dx=0.50}$ [ms]	$t_{\text{merger}}^{dx=0.375}$ [ms]	$t_{\text{merger}}^{dx=0.25}$ [ms]	$t_{\text{merger}}^{dx=0}(\text{ext})$ [ms]	$t_{\text{merger}}^{\text{EOB}}$ [ms]
SLy12vs12	9.22	11.76	13.61	15.07 ± 0.03	21.55
SLy13vs13	8.21	10.02	11.25	12.28 ± 0.04	17.25
SLy14vs14	6.72	8.27	9.50	10.39 ± 0.08	14.08
SLy15vs15	5.93	6.99	7.71	8.31 ± 0.02	11.64
SLy16vs16	5.00	6.13	6.81	7.44 ± 0.08	9.78
SLy135vs145	6.66	8.19	9.45	10.34 ± 0.10	14.09
SLy13vs15	6.52	7.91	9.31	10.14 ± 0.25	14.12
SLy125vs155	6.19	7.60	9.09	9.93 ± 0.29	14.21
SLy12vs16	5.52	7.26	8.73	9.75 ± 0.13	14.33
G275th14vs14	4.22	4.81	5.52	5.88 ± 0.17	13.63
G300th14vs14	7.63	9.69	10.55	11.67 ± 0.37	14.78

TABLE III. Computed merger time at different resolutions for the eleven BNS systems studied in the present work. In the fourth column is reported the extrapolated value at infinite resolution and in the fifth column the merger for a similar binary system with BHs instead of NSs computed using an EOB waveform.

the frequency of the corresponding BNS system. One can observe that the extrapolated merger time is always consistently lower than the approximation from an EOB for all models, with greater difference for the case of the only simulated model using the much softer G275th14v14 EOS (isentropic EOS $P = 30000\rho^{2.75}$ EOS).

This difference could be seen as an indication for the importance of tidal effects on the late stage of the merger, but it could also stem from possible differences in the initial data. We did not evolve a high enough number of orbits before the merger to draw any firm conclusion of which one is the case. In fact, the number of orbits we used (three to four) is quite low, and any contamination of the initial data would not have time to settle down completely, nor would a tidal effect be stabilized. We do plan to investigate this in future work using higher numbers of orbits.

Another interesting aspect besides the merger time is the emission of GW by the different models. In Figure 7 we show the overall waveform dynamics of all models at resolution $dx = 0.25$ CU. In particular, the bottom panels show the GW signal, while the energy flux radiated in GW, calculated according to Eq. (14), are shown in the middle. In the top panel we show the GW spectrum evaluated performing a Fourier transform of the data spanning the interval between 9 ms before and 11 ms after the merger time, after having multiplied the time domain signal with a Blackman window function. Our signal sampling has a Nyquist frequency of $\simeq 50.75$ kHz, and over the specified 20 ms interval, our spectrum has a resolution of $\simeq 45$ Hz.

The first noticeable result is that the general picture of a non-collapsing simulation with a $\Gamma = 3$ polytropic EOS and the one using the SLyPP EOS (with the same $\Gamma_{\text{th}} = 1.8$ thermal part) are very similar. From the right panel can be seen that both the GW energy emission and the spectrum nicely agree. This means that only the high-density section of the EOS is relevant for the

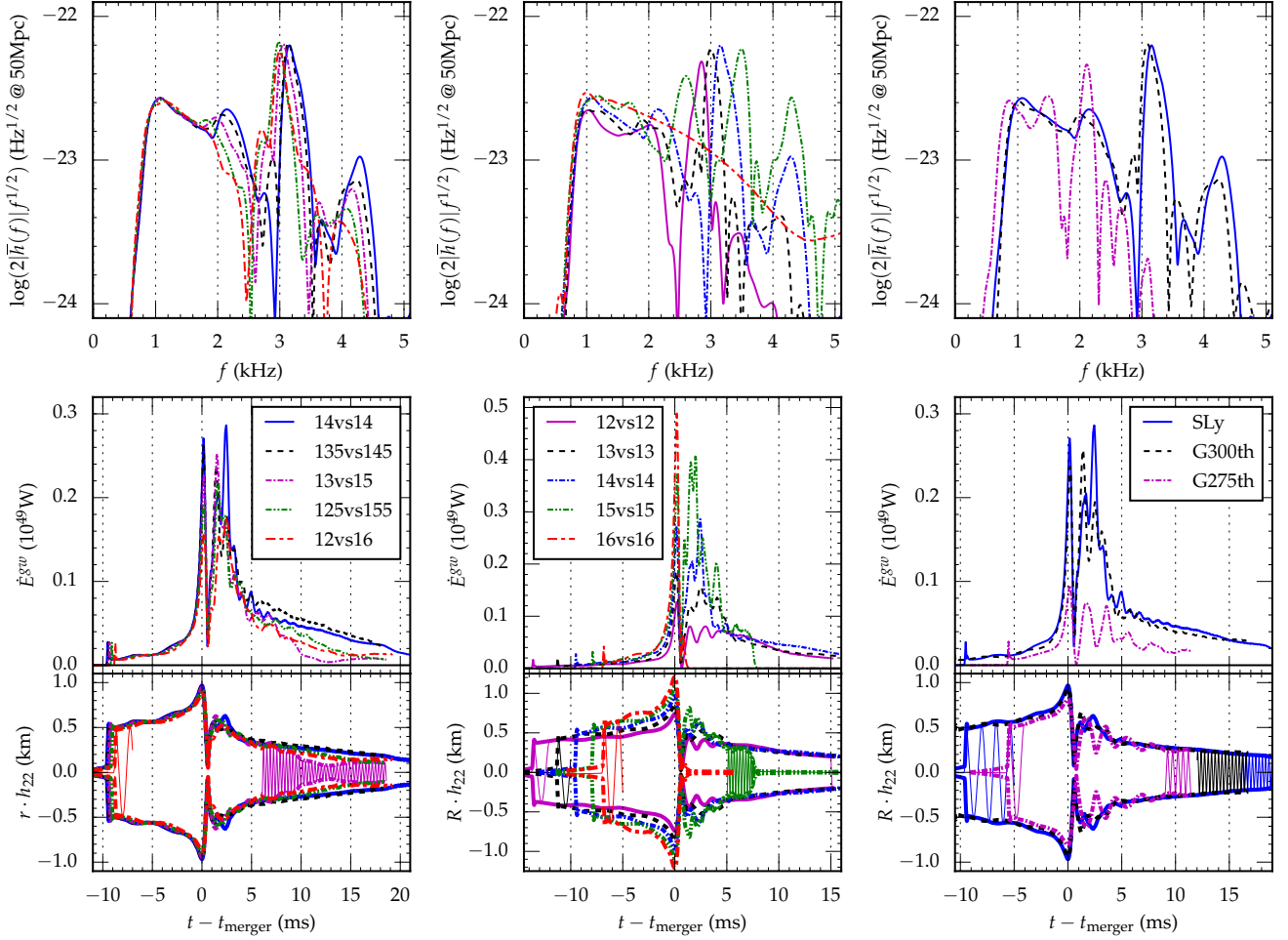


FIG. 7. Comparison of the unequal mass models (left), the equal mass models (center) and three models with the same baryonic mass but different EOS (on the right). The shown quantities are the same as in Figure 4: As there, they are aligned in time at their respective (different) merger times. The upper panels show the power spectral density (PSD) (Fourier-transform) of the effective GW signal $\bar{h}(f)$ in the optimal oriented case for a source at 50 Mpc, where it is considered the signal from $t_{\text{merger}} - 9$ ms to $t_{\text{merger}} + 11$ ms and a Blackman-windowing function has been applied. The second panel shows the total GW luminosity (energy flux). Finally, the bottom panel shows the envelope of the gravitational wave amplitudes and its real part, multiplied by the distance to the observer.

global behavior of the system (this is not true for models collapsing to a BH, as explained in section III D).

The GW spectrum shows the presence of a dominating peak for every model except for the promptly collapsing SLy16vs16. This peak is well-known in the literature and corresponds to the frequency f_p (also called f_2 or f_{peak}) of the fundamental quadrupolar $m = 2$ oscillation mode of the bar-deformed massive NS formed after the merger [65]. The frequency of this mode is related to the compactness of the star [66–70]. It increases for the more compact systems, as shown in panel 2 for different total mass models, and in panel 3 for different EOSs, where the $\Gamma = 2.75$ polytropic EOS is softer than the other two. It also has recently been correlated with the star’s tidal deformability [71] and the tidal coupling constant [72]. For the unequal mass case, we can only see a small depen-

dence on the mass ratio, with a higher frequency for the equal and the closest-to-equal mass models.

Secondary post-merger peaks at frequencies f_- and f_+ (also named as f_1 and f_3 in the literature) are also present and recognizable in the spectrum, which could be useful in extracting the NSs parameters (mass, radius) from future GW detections [9, 10]. The physical origin of these secondary frequencies is still debated. The first hypothesis formulated was to consider them as nonlinear combinations of the $m = 2$ and $m = 0$ oscillation modes of the hyper-massive NSs with the f_p frequency, since $f_p \simeq (f_- + f_+)/2$ and the difference $f_p - f_-$ is close to the quasi-radial oscillation frequency f_0 [65]. More recently, in [9, 10][73] they were attributed to the modulation of the main $m = 2$ frequency by the nonlinear radial oscillations of the two rotating stellar cores in the

Model	f_0 (kHz)	\tilde{f}_p (kHz)	f_p (kHz)	\hat{f} (kHz)	f_- (kHz)	f_+ (kHz)
SLy12vs12	1.30	2.80	2.85	-	-	-
SLy13vs13	1.30	2.91	3.00	-	1.88	4.13
SLy14vs14	1.18	3.17	3.15	-	2.14	4.29
G300th14v14	1.24	3.05	3.09	-	1.99	4.24
G275th14v14	1.01	2.10	2.11	1.56	-	-
SLy135vs145	1.17	3.16	3.14	2.84	2.05	4.24
SLy13vs15	1.23	3.04	3.05	2.82	1.95	4.16
SLy125vs155	1.25	3.01	2.98	2.72	1.79	4.07
SLy12vs16	1.27	3.02	3.00	2.71	-	-
SLy15vs15	0.81	3.50	3.49	-	2.59	4.30

TABLE IV. Main peak frequencies and damping times of the post-merger phase of the simulated models at $dx = 0.25 M_\odot$. The frequency of the f_0 and \tilde{f}_p peaks is determined by a single-frequency fitting procedure, while the others are derived by an analysis of the Fourier spectrum. Both ways to obtain the frequency have, using our current methods and resolutions, errors of about 50 – 100 Hz. The values obtained using different resolutions and reconstruction methods are within the error on the estimation of frequency differences. Indeed the data do not explicitly show any dependency of the peak frequency on resolution and methods.

first few milliseconds after the merger. Finally, in [74], two different concurrent mechanisms were proposed for the origin of the low frequency peak: the nonlinear combination of $m = 2$ and $m = 0$ modes at f_- (dominant in the more compact models), and the GW emission at $f = f_{\text{spiral}}$ from the spiral arms created by a strong deformation during the merger. These rotate in the inertial frame slower than the central cores, at a frequency $\frac{f_{\text{spiral}}}{2}$, and this effect would be dominant for less compact models. Our present data, however, are not sufficient to clarify which hypothesis is correct.

In Table IV we report the frequencies of all clearly recognizable spectral peaks for models shown in Figure 7. We also report the frequency f_0 of the quasi-radial mode, calculated using a fit starting at the time of the minimum value of the lapse α , and using a quadratic trial function with a superimposed damped oscillation:

$$\alpha_{\min} = a_2 t^2 + a_1 t + a_0 + A_0 e^{-\frac{t}{\tau_0}} \sin(2\pi f_0 t + \phi_0). \quad (16)$$

The frequency of the dominant mode \tilde{f}_p of the star after the merger is obtained by fitting the GW signal h_+ with a single oscillation mode with exponentially decaying amplitude

$$h_+ = A_p e^{-\frac{t}{\tau_p}} \sin(2\pi \tilde{f}_p t + \phi), \quad (17)$$

starting 5 ms after the merger, and waiting for the damping of sub-dominant modes, which happens on a timescale $\tau_0 \simeq 2 - 3$ ms (except for model SLy15vs15, for which we started the fit at 2 ms after the merger to have a large enough time window before the collapse).

The reported frequencies for the dominant and sub-dominant modes are obtained by interpolating the

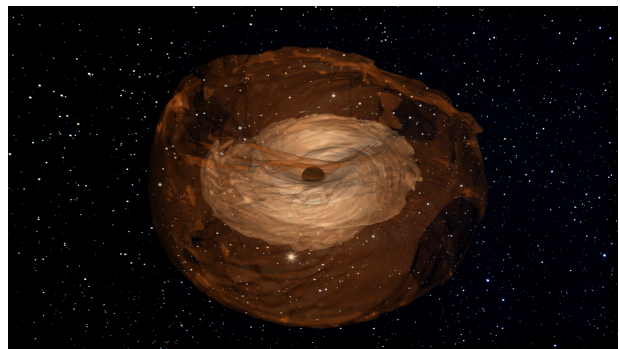


FIG. 8. Three-dimensional visualization of the disk-like remnant just after black hole formation ($t = 15.84$ ms). At this stage, the matter shown here is still above the neutron-drip threshold, but it will later drop to lower densities (See Fig. 9-left).

Fourier transform of the signal with a cubic spline, in order to obtain a frequency resolution of less than 50 Hz (i.e., of the resolution of the Fourier transform on a 20 ms interval), and then taking its maximum in an interval close to each visible peak.

Most models show the sub-dominant peaks at frequencies f_- and f_+ , close to the central f_p , with a maximum difference of the order of $\simeq 1$ kHz. At the same time, those frequency differences are of the same order of f_0 , with an error $||f_p - f_{+/-} - f_0||$ around 100 – 200 Hz.

We can see that in the unequal mass models the secondary peaks f_-, f_+ have a lower frequency and contain less power with increasing mass difference, as was previously already reported with only one model in [75]. We do not find a symmetric double-core structure with spiral arms right after the merger, but instead a tidal tail, generated from the capture of the less massive star outside and the heavier star's core rotating around the center of symmetry, as can be seen in Figure 6. Additionally, in those unequal mass models another low frequency peak (indicated with \hat{f} in Table IV) is present, closer to the dominant frequency f_p . This could be related to the f_{spiral} peak of [74], but further analysis is necessary to clarify its physical origin. For the equal mass case, increasing power in the secondary frequencies can be seen for the more massive systems (in accordance with [9]), while for the less compact models (SLy12vs12) the post-merger GW emission is characterized only by the single f_p frequency. Finally, the softer EOS model G275th14vs14 shows an important secondary peak at $\hat{f} = 1.56$ kHz, while no corresponding peak at $f_+ \simeq 2f_p - \hat{f}$ is present, and the difference $f_p - \hat{f}$ is not close to f_0 . This is again consistent with the f_{spiral} picture predicted in [74] for less compact stars.

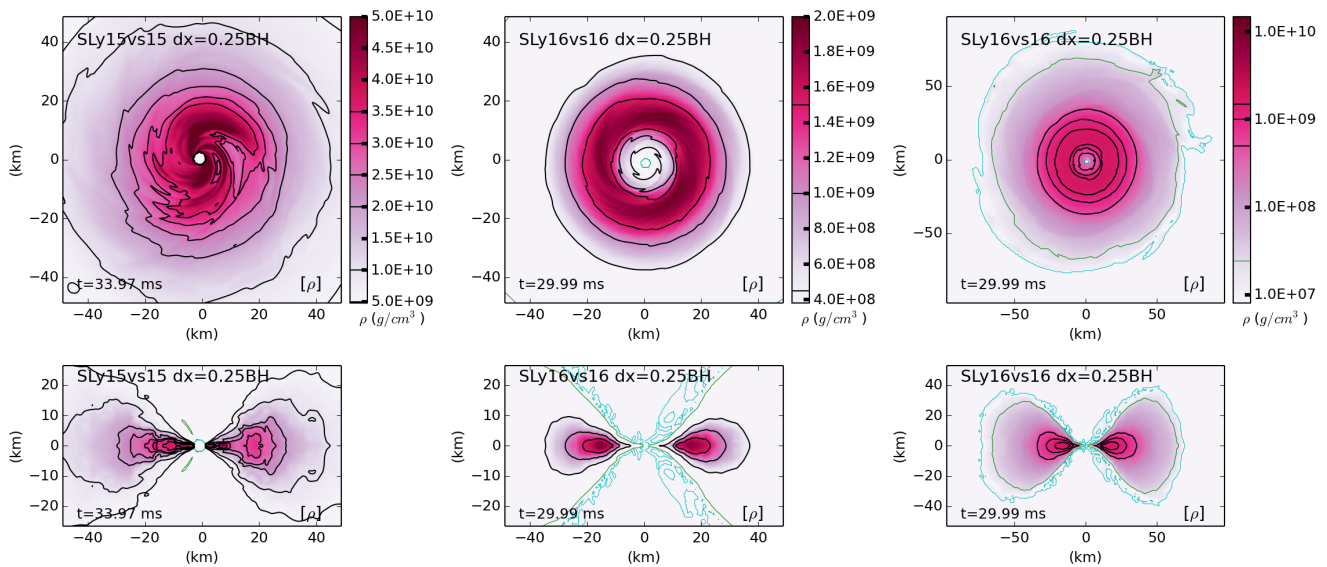


FIG. 9. Snapshot of the disk-like matter distribution in the $x-y$ plane (top) and $x-z$ plane (bottom) around the back hole at the final stage of the simulation. Model SLy15vs15 is shown on the left, while for model SLy16vs16 two different zoom levels are chosen in the center and on the right. The cyan outline in these two plots denotes the boundary of the atmosphere for this model: all matter from the initial binary system is still inside this region. The same cannot be said for model SLy15vs15, where a very low-density matter flow reaches the outer boundary and leaves the computational domain.

D. Models Resulting in Collapse to a Black Hole

As previously noted, the evolution of model SLy16vs16 results in a direct collapse and the formation of a BH just after the merger. Model SLy15vs15, instead, is characterized by a delayed collapse to a BH a few milliseconds after merger, as shown in Figures 8 and 9. One of the main characteristics of our results for these two models is that after the merger and subsequent collapse to a BH, the remaining matter density drops quickly below neutron drip. Our simulations do not include a proper neutron-proton treatment and not even Neutrino emission. Nevertheless, the fact that the remnant matter is below the neutron drip threshold is an indication that a noticeable emission of neutrinos should occur within the 10 ms that follows the merger (see Figure 10) and of the importance of the study of the r-process that may occur in neutron star mergers and on the necessity to use real Nuclear Physics EOS in the study of the post-merger phase.

In more detail, we observe prompt BH formation for model SLy16vs16 with the appearance of an apparent horizon at $t = 6.94$ ms and $t = 7.60$ ms for resolutions $dx = 0.375$ and $dx = 0.25$ CU, respectively, less than 1 ms after merger. For model SLy15vs15, the BH formation is delayed, at simulation times of $t = 18.81$ ms and $t = 15.35$ ms for resolutions $dx = 0.375$ and $dx = 0.25$ CU, respectively, resulting in a delay of 11.8 ms and 7.4 ms after the merger. This model (with a total baryonic mass of $3.0M_{\odot}$ and an initial ADM mass of $2.697M_{\odot}$, as reported in Table II) is close to one often analyzed in the published literature (with total baryonic mass $2.989M_{\odot}$

and initial ADM mass $2.675M_{\odot}$) [9, 70, 75], so a direct comparison of the collapse times is possible. In [9, 10], also using a BSSN-NOK spacetime evolution scheme, but employing PPM reconstruction, using only the four highest density polytropic pieces of the SLyPP EOS (see Table I) used in the present work, and setting $\Gamma_{th} = 2.0$, no collapse to BH was found in the first 25 ms after the merger. Using the same setup, with the only difference of $\Gamma_{th} = 1.8$, in [70] a collapse to a BH was found about 10 ms after the merger. In the same paper, the authors also note that for a different model an increase of Γ_{th} significantly delays the collapse. In [75], using the Z4c formulation of Einstein's equations and WENO reconstruction, with the same EOS of [70], a quite long NS lifetime of 13 ms after the merger is reported. These differences indicate the need for a careful study of the influence of the numerical evolution schemes, but more so the dependency of the collapse on the EOS details, especially the adiabatic index at low densities and the choice of Γ_{th} . Even small differences in these choices could potentially lead to different predictions for the estimated total energy emission in gravitational waves, and with that, their detectability.

Unlike for the inspiral phase (see Section III B), we are not able to do a complete study of the convergence properties during the post-merger and collapse phase, e.g. for the neutron star life time, without using a higher resolution (incurring a higher computational cost). Model SLy16vs16 is promptly collapsing after the merger at all resolutions, even as low as $dx = 0.75$ CU. Model SLy15vs15, instead, shows no collapse for $dx = 0.75$ CU even 49 ms after the merger, while the neutron star col-

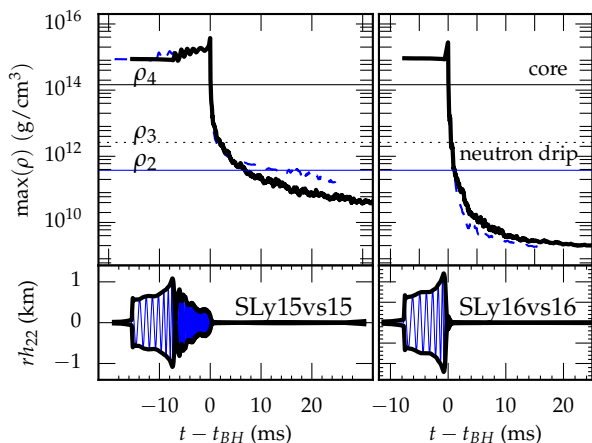


FIG. 10. Top panels: maximum density $\max(\rho)$ of the matter remaining on the numerical grid outside of the horizon as a function of the time, for both models that show BH formation. As can be seen, after the formation of the BH, densities drop quickly below neutron drip, which an EOS has to describe appropriately to obtain reasonable results. Bottom panel: GW envelope for waves emitted by both models. While an extended emission from the hyper-massive neutron star is visible for model SLy15vs15, the prompt collapse in model SLy16vs16 cuts off emission shortly after merger besides a comparatively short and weak BH ring-down.

lapses at 6.11 ms, 11.81 ms, and 7.36 ms after merger at resolutions $dx = 0.50$, $dx = 0.375$, and $dx = 0.25$ CU, respectively. Further analysis would be necessary to fully establish robust convergence for the collapse time in similar models. We will leave a detailed study of this point to future work.

In order to characterize the dynamics of these configurations we found it useful to analyze two quantities that can be easily extracted from simulation data: the mass and/or energy, and the angular momentum along the z -axis, assuming an axial and temporal symmetry. The latter condition is indeed approximately reached at the end of the presented simulations. These quantities are defined in terms of the two vectors $\xi_{(t)}^\mu = (1, 0, 0, 0)$ and $\xi_{(\phi)}^\mu = (0, \cos(\phi), \sin(\phi), 0)$ (see 8), and are the same that were also used in [22, 23] to characterize the properties of isolated rotating stars. Namely:

$$M = - \int (2T_\nu^\mu - \delta_\nu^\mu T_\alpha^\alpha) \xi_{(t)}^\nu d^3\Sigma_\mu \quad (18)$$

$$J_z = \int T_\nu^\mu \xi_{(\phi)}^\nu d^3\Sigma_\mu, \quad (19)$$

where Σ_μ are the 3-dimensional slices of fixed coordinate time t ($d^3\Sigma_\mu = \sqrt{\gamma}d^3x$). To obtain the energy and angular momentum budgets of the collapsed models we used the energy (E^{gw}) and angular momentum (J_z^{gw}) carried away by gravitational radiation (see Eqs. (14) and (15)), and the mass M_{bh} and angular

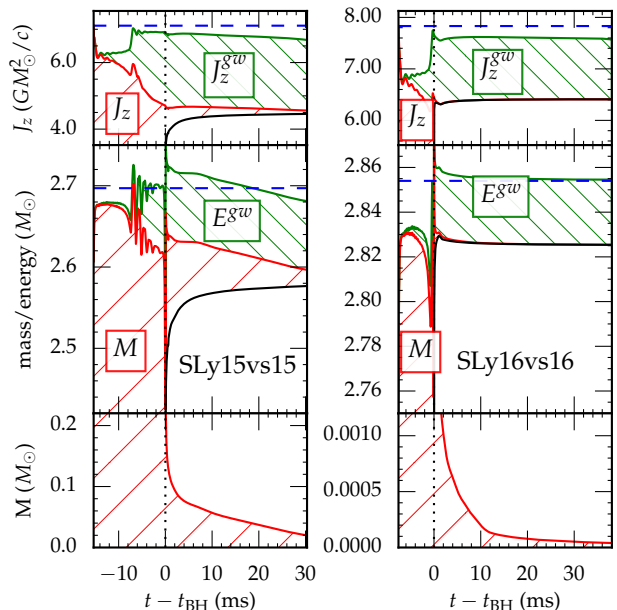


FIG. 11. Angular momentum and mass budget for the evolution of models SLy15vs15 (left) and SLy16vs16 (right). The blue, dashed, horizontal line indicates the ADM mass of the initial data, as calculated by Lorene. The red area (hatched from the bottom left to the top right) shows the contribution from matter left on the grid, while the green area, hatched from the top left to the bottom right, shows contributions from emitted GW, plotted in retarded time with regard to the position of the detector, assuming emission from the origin. The bottom-most, black, solid line indicates the angular momentum and mass of the BH. For both models, the sum of these three contributions remains close during the entire evolution.

momentum of the BH J_{bh} , computed using the isolated horizon formalism [76–78] (provided by the module `QuasiLocalMeasures` [79]) on the the apparent horizon (located by the module `AHFinderDirect` [80]). The results are shown in Fig. 11.

For the quickly collapsing model SLy16vs16 we found, 25 ms after the collapse, a mass of $\approx 2.83M_\odot$ and an angular momentum of $\approx 6.41 GM_\odot^2/c$, while the total (gravitational) mass still present in the disk is only around $6.19 \cdot 10^{-5}M_\odot$. In contrast, we found for model SLy15vs15, also 25 ms after the collapse, a BH mass of $2.57M_\odot$ and an angular momentum of $4.45 GM_\odot^2/c$, while the remaining matter is either escaping the grid (very low density), or is still forming and driving an accretion disk. The total remaining mass on the grid amounts to about $0.028M_\odot$, and its density is below the neutron drip threshold.

IV. CONCLUSIONS

We have presented a study of BNS mergers for equal and unequal mass systems with the semi-realistic seven-

segment piece-wise polytropic SLyPP EOS with a thermal component of $\Gamma_{th} = 1.8$. All our results have been produced using open source and freely available software, the Einstein Toolkit for the dynamical evolution and the LORENE library for generating the initial models. Namely, we studied five equal-mass and four unequal-mass models with total ADM mass in the range between $2.207 M_{\odot}$ and $2.854 M_{\odot}$, and a mass ratio $q = M^{(1)}/M^{(2)}$ as low as 0.77. The dynamics of all simulated models started with the stars at a separation of 40 km. We followed this late-inspiral phase and the after-merger phase for more than 20 ms after merger.

We analyzed the merger and post-merger phase of BNS evolution in detail, studying their gravitational wave emission, the radiated energy and angular momentum and the gravitational waves spectrum. We investigated the differences between equal-mass models and unequal mass ones. In the first case a bar-deformed hyper-massive NS is produced after the merger (for all models except SLy16vs16 which promptly collapses to a BH) with symmetrical spiral arms and a rotating double-core structure. After a relaxation period of some milliseconds the star reaches its final state where only the fundamental $m = 2$ mode is excited. Unequal mass models, instead, show after the merger a single arm structure created by the tidal deformation of the less massive star. This qualitative difference leads also to differences in the GW spectrum, with the suppression of modes linked to the quasi-radial oscillations and the presence of a new sub-dominant mode, closer in frequency to the dominant $m = 2$ excitation.

Of all simulated models two collapse to a BH, one right after the merger (SLy16vs16), and one after a short hyper-massive NS phase (SLy15vs15). For both models a leftover accretion disk is present, with matter density under the neutron drip limit. This means that a correct form of the low density-section of the EOS should be important for the description of the disk and matter surrounding the remnant BH.

We studied the convergence properties of the numerical evolution in the inspiral phase, focusing on the value of the merger time computed for simulations with different resolutions and different numerical methods. We tried three different methods for the reconstruction of hydrodynamical variables (WENO, PPM and MP5) and two different evolution schemes for the gravitational sector (BSSN-NOK and CCZ4). The merger time showed second order convergence, and our results for the different methods, for resolution $dx = 0.25$ CU and better, do agree. We have explicitly shown that we achieve second-order convergence in the inspiral phase when PPM or WENO reconstruction is combined with the BSSN-NOK methods. In the other two cases we find that a much higher resolution is needed to explicitly show that a similar order-two convergence is present. Our result seems to indicate that to achieve reliable results at lower resolutions the combined use of BSSN-NOK and WENO seems the best setup, out of the ones we tested. This

analysis allowed us to extrapolate the merger time for all simulated models for infinite resolution $dx = 0$.

In addition, we compared to two BNS models of the same total baryonic mass ($M_0 = 2.8 M_{\odot}$) as model SLy14vs14 but with only one piece-wise component, and the same thermal part but different stiffness. The first model, G300th14vs14, has the same average stiffness ($\Gamma = 3.00$) as the SLyPP EOS, while the other model, G275th14vs14, shows a softer average stiffness ($\Gamma = 2.75$), which is similar to Shen EOS (see [23]). Using these, we find that the merger time increased only by a fraction (from 10.4 ms to 11.7 ms) in the case of G300th14vs14, while it is significantly decreased (from 10.4 ms to 5.9 ms) in the case of the softer G275th14vs14 model, which we attribute to the expectation that tidal effects are greater when the deformability of the star is increased (like in the case of softer stiffness). In the after-merger stage we observed only a small variation in the position of the peak for the gravitational wave emission in the first case, while the later model shows substantial differences to the SLy14vs14 comparison model.

ACKNOWLEDGMENTS

This project greatly benefited from the availability of public software that enabled us to conduct all simulations, namely “LORENE” and the “Einstein Toolkit”. We express our gratitude to the many people that contributed to their realization.

This work would have not been possible without the support of the SUMA INFN project that provided the financial support of the work of AF and the computer resources of the CINECA “GALILEO” HPC Machine, where most of the simulations were performed. Other computational resources were provided by the Louisiana Optical Network Initiative (QB2, allocations loni_hyrel, loni_numrel and loni_cactus), and by the LSU HPC facilities (SuperMike II, allocations hpc_hyrel and hpc_numrel). FL is directly supported by, and this project heavily used infrastructure developed using support from the National Science Foundation in the USA (Grants No. 1212401, No. 1212426, No. 1212433, No. 1212460). Partial support from INFN “Iniziativa Specifica TEONGRAV” and by the “NewCompStar”, COST Action MP1304, are kindly acknowledged.

We also graciously thank Dennis Castleberry for proof-reading the manuscript.

Appendix A: Computational Cost

The implementation of any computational intensive research program like the one developed in the present work needs a careful analysis of the computational cost of the simulations (the number of CPU core hours needed to perform each simulation) and a careful management of resources. In that, speed, and with that total runtime,

Level	$\min(x/y)$ (CU)	$\max(x/y)$ (CU)	$\min(z)$ (CU)	$\max(z)$ (CU)	(N_x, N_y, N_z) $dx = 0.25$
1	-720	720	0	720	(185,185,96)
2	-360	360	0	360	(205,205,106)
3	-180	180	0	180	(205,205,106)
4	-90	90	0	90	(205,205,106)
5	-60	60	0	30	(265,265,76)
6	-30	30	0	15	(265,265,76)
(7	-15	15	0	7.5)	(265,265,76)

TABLE V. Simulation grid boundaries of refinement levels. Level 7 is only used for simulations forming a BH, once the minimum of the lapse $\alpha < 0.5$. Resolutions as reported in this paper always refer to grid 6.

Δx (CU)	0.75	0.50	0.375	0.25	0.185	0.125
# threads	16	64	128	256	512	2048
# MPI	2	8	16	32	64	256
Memory (GBytes)	3.8	19	40	108	237	768
speed (CU/h)	252	160	124	53	36	16
speed (ms/h)	1.24	0.78	0.61	0.26	0.18	0.08
cost (SU/ms)	13	81	209	974	2915	26053
total cost (kSU, 50 ms)	0.65	4	10.5	49	146	1300

TABLE VI. Computational cost of the simulations, for the example of using BSSN-NOK, with WENO reconstruction for the hydrodynamics. SU stands for service unit: one hour on one CPU core. The reported values refers to the ‘‘GALILEO’’ PRACE-Tier1 machine locate at CINECA (Bologna, Italy) equipped with 521 nodes, two-8 cores Haswell 2.40 GHz, with 128 GBytes/node memory and 4xQDR Infiniband interconnect. Also, these are only correct for evolutions that do not end with the formation of a BH, as an additional refinement level was used to resolve the BH surroundings, and more analysis quantities had to be computed (e.g., the apparent horizon had to be found). In addition, the simulations resulting in a BH were performed on facilities at Louisiana State University: SuperMike II (LSU HPC) and QB2 (Loni).

however, are not the only variables to consider. Required memory puts a lower bound on the size of the employed resources, while an upper bound is present at the breakdown of strong scaling.

To quantify these needs, the resolution and the size of the computational grid are most important. Table V shows the characteristics of the grid we used for the present work. In particular we use a fixed structure of mesh-refined, centered grids, with the exception of an additional refinement level for simulations resulting in an apparent horizon, and then only starting shortly before the merger (when the minimum of the lapse α on the grid dropped below 0.5). In the last column of Table V we show the actual grid-size in computation-points of each level, for resolution $dx = 0.25$ CU. Clearly the actual grid size (including ghost-zones and buffer-zones) changes varying with resolution, and is not explicitly shown here for that reason.

With the computational domain completely specified, the next step of an analysis of the computational cost is to asses the cost for a full simulation of a particular model at the desired resolution. Table VI shows the actual simulation cost as function of resolution, for a particular High-Performance-Computer (HPC) system used in the present research program, namely the ‘‘GALILEO’’ system installed at the Italian CINECA supercomputer center. As it was discussed in the conclusion, our result show that the combined use of BSSN-NOK and WENO allows the possibility to find qualitatively accurate results in agreement with high-resolutions simulations. This is a very desirable feature since it allows researchers to quickly scan numerous different models in order to select the most interesting for further study using higher resolution.

All of our results have been produced using open source and freely available software, the Einstein Toolkit for the dynamical evolution and the LORENE library for generating the initial models. That means that the whole set of our result can be reproduced and re-analyzed by re-running the simulation from a common code-base. Some modifications of the above mentioned software were necessary, but these changes are also open source, and are available for download from the University of Parma WEB web server of the gravitational group [81]. We kindly ask to cite this work if you find any of the material there useful for your own research.

-
- | | |
|--|--|
| <p>[1] J. Aasi <i>et al.</i> (LIGO Scientific), <i>Class. Quant. Grav.</i> 32, 074001 (2015), arXiv:1411.4547 [gr-qc].</p> <p>[2] F. Acernese <i>et al.</i> (VIRGO), <i>Class. Quant. Grav.</i> 32, 024001 (2015), arXiv:1408.3978 [gr-qc].</p> <p>[3] B. P. Abbott <i>et al.</i> (Virgo, LIGO Scientific), <i>Phys. Rev. Lett.</i> 116, 061102 (2016), arXiv:1602.03837 [gr-qc].</p> <p>[4] LIGO Scientific Collaboration, Virgo Collaboration, J. Aasi, J. Abadie, B. P. Abbott, R. Abbott, T. D. Abbott, M. Abernathy, T. Accadia, F. Acernese, and et al., ArXiv e-prints (2013), arXiv:1304.0670 [gr-qc].</p> <p>[5] J. Abadie <i>et al.</i> (VIRGO, LIGO Scientific), <i>Class. Quant. Grav.</i> 27, 173001 (2010), arXiv:1003.2480 [astro-ph.HE].</p> <p>[6] A. Buonanno and T. Damour, <i>Phys. Rev.</i> D59, 084006 (1999), arXiv:gr-qc/9811091 [gr-qc].</p> | <p>[7] T. Damour and A. Nagar, <i>Physical Review D</i> 81, 084016 (2010).</p> <p>[8] D. Bini, T. Damour, and G. Faye, <i>Physical Review D</i> 85, 124034 (2012).</p> <p>[9] K. Takami, L. Rezzolla, and L. Baiotti, <i>Phys. Rev.</i> D91, 064001 (2015), arXiv:1412.3240 [gr-qc].</p> <p>[10] K. Takami, L. Rezzolla, and L. Baiotti, <i>Proceedings, Spanish Relativity Meeting: Almost 100 years after Einstein Revolution (ERE 2014)</i>, <i>J. Phys. Conf. Ser.</i> 600, 012056 (2015).</p> <p>[11] F. Douchin and P. Haensel, <i>Astron. Astrophys.</i> 380, 151 (2001), arXiv:astro-ph/0111092.</p> <p>[12] J. S. Read, B. D. Lackey, B. J. Owen, and J. L. Friedman, <i>Physical Review D</i> 79, 124032 (2009).</p> |
|--|--|

- [13] A. Harten, B. Engquist, S. Osher, and S. R. Chakravarthy, *J. Comp. Phys.* **71**, 231 (1987).
- [14] C. W. Shu, in *High order methods for computational physics*, edited by T. J. Barth and H. A. Deconinck (Springer, New York, 1999) pp. 439–582.
- [15] T. Nakamura, K. Oohara, and Y. Kojima, *Prog. Theor. Phys. Suppl.* **90**, 1 (1987).
- [16] M. Shibata and T. Nakamura, *Phys. Rev. D* **52**, 5428 (1995).
- [17] T. W. Baumgarte and S. L. Shapiro, *Phys. Rev. D* **59**, 024007 (1999), arXiv:gr-qc/9810065.
- [18] M. Alcubierre, B. Brügmann, T. Dramlitsch, J. A. Font, P. Papadopoulos, E. Seidel, N. Stergioulas, and R. Takahashi, *Phys. Rev. D* **62**, 044034 (2000), arXiv:gr-qc/0003071.
- [19] M. Alcubierre, B. Brügmann, P. Diener, M. Koppitz, D. Pollney, E. Seidel, and R. Takahashi, *Phys. Rev. D* **67**, 084023 (2003), arXiv:gr-qc/0206072.
- [20] D. Alic, C. Bona-Casas, C. Bona, L. Rezzolla, and C. Palenzuela, *Phys. Rev. D* **85**, 064040 (2012), arXiv:1106.2254 [gr-qc].
- [21] F. Löffler, J. Faber, E. Bentivegna, T. Bode, P. Diener, R. Haas, I. Hinder, B. C. Mundim, C. D. Ott, E. Schnetter, G. Allen, M. Campanelli, and P. Laguna, *Class. Quantum Grav.* **29**, 115001 (2012), arXiv:1111.3344 [gr-qc].
- [22] R. De Pietri, A. Feo, L. Franci, and F. Löffler, *Phys. Rev. D* **90**, 024034 (2014), arXiv:1403.8066 [gr-qc].
- [23] F. Löffler, R. De Pietri, A. Feo, F. Maione, and L. Franci, *Phys. Rev. D* **91**, 064057 (2015), arXiv:1411.1963 [gr-qc].
- [24] A. Bauswein, H.-T. Janka, and R. Oechslin, *Physical Review D* **82**, 084043 (2010).
- [25] E.ourgoulhon, P. Grandclement, K. Taniguchi, J.-A. Marck, and S. Bonazzola, *Phys. Rev. D* **63**, 064029 (2001), arXiv:gr-qc/0007028.
- [26] LORENE, “LORENE: Langage Objet pour la RELativité Numérique,” <http://www.lorene.obspm.fr/>.
- [27] EinsteinToolkit, “Einstein Toolkit: Open software for relativistic astrophysics,” <http://einstein toolkit.org/>.
- [28] Cactus developers, “Cactus Computational Toolkit,” <http://www.cactuscode.org/>.
- [29] T. Goodale, G. Allen, G. Lanfermann, J. Massó, T. Radke, E. Seidel, and J. Shalf, in *Vector and Parallel Processing – VECPAR’2002, 5th International Conference, Lecture Notes in Computer Science* (Springer, Berlin, 2003).
- [30] G. Allen, T. Goodale, G. Lanfermann, T. Radke, D. Rideout, and J. Thornburg, *Cactus Users’ Guide* (2011).
- [31] E. Schnetter, S. H. Hawley, and I. Hawke, *Class. Quantum Grav.* **21**, 1465 (2004), arXiv:gr-qc/0310042.
- [32] E. Schnetter, P. Diener, E. N. Dorband, and M. Tiglio, *Class. Quantum Grav.* **23**, S553 (2006), arXiv:gr-qc/0602104.
- [33] Carpet, Carpet: Adaptive Mesh Refinement for the Cactus Framework, <http://www.carpetcode.org/>.
- [34] L. Baiotti, I. Hawke, P. J. Montero, F. Löffler, L. Rezzolla, N. Stergioulas, J. A. Font, and E. Seidel, *Phys. Rev. D* **71**, 024035 (2005), arXiv:gr-qc/0403029.
- [35] I. Hawke, F. Löffler, and A. Nerozzi, *Phys. Rev. D* **71**, 104006 (2005), arXiv:gr-qc/0501054.
- [36] P. Mösta, B. C. Mundim, J. A. Faber, R. Haas, S. C. Noble, T. Bode, F. Löffler, C. D. Ott, C. Reisswig, and E. Schnetter, *Classical and Quantum Gravity* **31**, 015005 (2014), arXiv:1304.5544 [gr-qc].
- [37] McLachlan, “McLachlan, a public BSSN code,” <http://www.cct.lsu.edu/~eschnett/McLachlan/>.
- [38] S. Husa, I. Hinder, and C. Lechner, *Comput. Phys. Commun.* **174**, 983 (2006), arXiv:gr-qc/0404023.
- [39] C. Lechner, D. Alic, and S. Husa, *Analele Universitatii de Vest din Timisoara, Seria Matematica-Informatica* **42** (2004), arXiv:cs/0411063.
- [40] Kranc, “Kranc: Kranc assembles numerical code,” <http://kranccode.org/>.
- [41] C. Runge, *Mathematische Annalen* **46**, 167 (1895).
- [42] W. Kutta, *Z. Math. Phys.* **46**, 435 (1901).
- [43] A. Harten, P. D. Lax, and B. van Leer, *SIAM review* **25**, 35 (1983).
- [44] B. Einfeldt, *SIAM J. Numer. Anal.* **25**, 294 (1988).
- [45] P. Colella and P. R. Woodward, *J. Comp. Phys.* **54**, 174 (1984).
- [46] D. Radice and L. Rezzolla, *Journal of Computational Physics* **136**, 83–99 (1997).
- [47] E. Newman and R. Penrose, *Journal of Mathematical Physics* **3**, 566 (1962).
- [48] T. Regge and J. A. Wheeler, *Phys. Rev.* **108**, 1063 (1957).
- [49] F. J. Zerilli, *Phys. Rev. Lett.* **24**, 737 (1970).
- [50] V. Moncrief, *Annals Phys.* **88**, 323 (1974).
- [51] J. G. Baker, M. Campanelli, and C. O. Lousto, *Phys. Rev. D* **65**, 044001 (2002), arXiv:gr-qc/0104063.
- [52] T. Damour, A. Nagar, M. Hannam, S. Husa, and B. Brügmann, *Physical Review D* **78**, 044039 (2008).
- [53] C. Reisswig and D. Pollney, *Classical and Quantum Gravity* **28**, 195015 (2011).
- [54] L. Baiotti, S. Bernuzzi, G. Corvino, R. De Pietri, and A. Nagar, *Physical Review D* **79**, 024002 (2009).
- [55] E. Berti, V. Cardoso, J. A. González, U. Sperhake, M. Hannam, S. Husa, and B. Brügmann, *Physical Review D* **76**, 064034 (2007).
- [56] H. Nakano, J. Healy, C. O. Lousto, and Y. Zlochower, *Physical Review D* **91**, 104022 (2015).
- [57] B. Brügmann, J. A. González, M. Hannam, S. Husa, U. Sperhake, and W. Tichy, *Physical Review D* **77**, 024027 (2008).
- [58] D. Alic, W. Kastaun, and L. Rezzolla, *Phys. Rev. D* **88**, 064049 (2013), arXiv:1307.7391 [gr-qc].
- [59] M. Ruiz, D. Hilditch, and S. Bernuzzi, *Phys. Rev. D* **83**, 024025 (2011), arXiv:1010.0523 [gr-qc].
- [60] K. Hotokezaka, K. Kyutoku, H. Okawa, and M. Shibata, *Physical Review D* **91**, 064060 (2015).
- [61] A. Kurganov and E. Tadmor, *Journal of Computational Physics* **160**, 241 (2000).
- [62] C. Palenzuela, S. L. Liebling, D. Neilsen, L. Lehner, O. Caballero, E. O’Connor, and M. Anderson, *Physical Review D* **92**, 044045 (2015).
- [63] D. Radice, L. Rezzolla, and F. Galeazzi, (2015), arXiv:1502.00551 [gr-qc].
- [64] The EOB waveform has been obtained through the publicly available LALSUIT LIGO/Virgo software (“[git://versions.ligo.org/lalsuite.git](https://versions.ligo.org/lalsuite.git)”) using the utility: “[/lalsim-inspiral -a EOBNRv2 \[options\]](#)”.
- [65] N. Stergioulas, A. Bauswein, K. Zagkouris, and H.-T. Janka, *Monthly Notices of the Royal Astronomical Society* **418**, 427 (2011).
- [66] K. Hotokezaka, K. Kyutoku, H. Okawa, and M. Shibata, *Phys. Rev. D* **91**, 064060 (2015), arXiv:1502.03457 [gr-qc].
- [67] A. Bauswein, N. Stergioulas, and H.-T. Janka, *Physical*

- Review D **90**, 023002 (2014).
- [68] A. Bauswein and H.-T. Janka, Physical review letters **108**, 011101 (2012).
- [69] A. Bauswein, N. Stergioulas, and H.-T. Janka, (2015), arXiv:1508.05493.
- [70] K. Hotokezaka, K. Kiuchi, K. Kyutoku, T. Muranushi, Y.-i. Sekiguchi, M. Shibata, and K. Taniguchi, Physical Review D **88**, 044026 (2013).
- [71] J. S. Read, L. Baiotti, J. D. Creighton, J. L. Friedman, B. Giacomazzo, K. Kyutoku, C. Markakis, L. Rezzolla, M. Shibata, and K. Taniguchi, Physical Review D **88**, 044042 (2013).
- [72] S. Bernuzzi, T. Dietrich, and A. Nagar, Phys. Rev. Lett. **115**, 091101 (2015), arXiv:1504.01764 [gr-qc].
- [73] W. Kastaun and F. Galeazzi, Physical Review D **91**, 064027 (2015).
- [74] A. Bauswein and N. Stergioulas, Phys. Rev. **D91**, 124056 (2015), arXiv:1502.03176 [astro-ph.SR].
- [75] T. Dietrich, S. Bernuzzi, M. Ujevic, and B. Brügmann, Phys. Rev. **D91**, 124041 (2015), arXiv:1504.01266 [gr-qc].
- [76] A. Ashtekar, C. Beetle, O. Dreyer, S. Fairhurst, B. Krishnan, J. Lewandowski, and J. Wisniewski, Phys. Rev. Lett. **85**, 3564 (2000), arXiv:gr-qc/0006006 [gr-qc].
- [77] A. Ashtekar, C. Beetle, and J. Lewandowski, Class. Quant. Grav. **19**, 1195 (2002), arXiv:gr-qc/0111067 [gr-qc].
- [78] A. Ashtekar and B. Krishnan, Living Rev. Rel. **7**, 10 (2004), arXiv:gr-qc/0407042 [gr-qc].
- [79] O. Dreyer, B. Krishnan, D. Shoemaker, and E. Schnetter, Phys. Rev. D **67**, 024018 (2003), arXiv:gr-qc/0206008.
- [80] J. Thornburg, Class. Quantum Grav. **21**, 743 (2004), arXiv:gr-qc/0306056.
- [81] See the University of Parma Gravity group WEB page: www.fis.unipr.it/gravity/Research/BNS2015.html.